RESEARCH ARTICLE

Heat-Transfer Gain Versus Irreversibility Cost in a Radiative MHD Tri-Hybrid Nanofluid Thin Film: An Equal-Loading Second-Law Assessment

Muhammad Riaz Khan[1,*] **and Noor Aslam Khan**[2,*]

[1] Department of Mathematics, King Fahd University of Petroleum and Minerals, Dhahran 31261, Saudi Arabia
[2] Department of Mathematical Sciences, University of Lakki Marwat, Lakki Marwat, Khyber Pakhtunkhwa, Pakistan

Abstract

Comparisons among mono-, binary- and ternary nanofluids often change the particle set and the total solid loading at the same time, so the effect of composition cannot be told apart from that of concentration. We recalculate an unsteady radiative magnetohydrodynamic (MHD) CuO-TiO_2-SiO_2/blood thin film with the same total particle volume fraction in every suspension. The finite free surface is found by shooting with fourth-order Runge-Kutta integration and checked with an independent collocation code. At a total particle fraction of 3%, replacing SiO_2/blood by the ternary suspension raises the reduced wall heat-transfer rate by 0.881%, the wall-drag measure by 2.029% and the integrated entropy measure by 0.668%. The shooting benchmark agrees with the classical finite-film solution to within 9.55×10^{-4}%, and on the production grid ($N_c = 48$) shooting and collocation differ by at most 0.0432% in the reported wall quantities at the reference state. The spread produced by alternative conductivity constructions is smaller than the heat-transfer increment. Magnetic forcing, film unsteadiness and radiation change the response far more than particle substitution does. Under equal loading, the ternary mixture therefore gives a small thermal gain at the price of a larger relative drag penalty.

Keywords: tri-hybrid nanofluid, thin-film flow, entropy generation, nonlinear thermal radiation, magnetohydrodynamics, equal solid loading.

1 Introduction

For a stretching-sheet film, the liquid domain ends at a free surface rather than at a prescribed far-field boundary. The interface $y = h(t)$ is material: the tangential stress vanishes there, and the kinematic condition fixes its normal velocity. The film thickness $h(t)$ is therefore obtained together with the velocity field and is not prescribed independently. Andersson et al. [1] formulated the unsteady stretching-film problem, Wang [2] treated the finite similarity interval,

Submitted: 13 August 2026
Revised: 26 September 2026
Accepted: 11 October 2026
Published: 28 November 2026

Vol. 3, **No.** 1, 2027.
10.62762/IJTSSE.2026.306879

***Corresponding authors:**
✉ Muhammad Riaz Khan
mrkhan.math@gmail.com
✉ Noor Aslam Khan
na.math.qau@gmail.com

Citation
Khan, M. R., & Khan, N. A. (2026). Heat-Transfer Gain Versus Irreversibility Cost in a Radiative MHD Tri-Hybrid Nanofluid Thin Film: An Equal-Loading Second-Law Assessment. *International Journal of Thermo-Fluid Systems and Sustainable Energy*, 3(1), 14–30.

© 2026 by the Authors. Published by Institute of Central Computation and Knowledge. This is an open access article under the CC BY license (https://creativecommons.org/licenses/by/4.0/).

and Liu and Andersson [3] examined its heat transfer. Magnetic, thermocapillary, internal-heating, dissipative and radiative effects were later added to the same class of flows [4–6]. The moving endpoint matters here because a momentum perturbation changes both the wall gradient and the available film thickness.

Comparing mono-, binary- and ternary suspensions requires a separate control on the amount of solid. If the particle set and the total volume fraction are changed together, a composition effect is mixed with a concentration effect, and the latter alters viscosity, density, volumetric heat capacity and conductivity even when the relative particle proportions stay fixed. Rabby et al. [7] reviewed the concentration dependence of tri-hybrid properties. The measurements of Mousavi et al. [8] on $CuO/CaCO_3/SiO_2$-water mixtures vary both total concentration and particle ratio. Their carrier fluid and geometry differ from the present film, but the experimental point is the same: composition cannot be isolated unless the total dispersed volume is fixed.

Recent studies also show why a small heat-transfer increment cannot be judged from Nu alone. Jan et al. [9] studied the drag and forced-convection response of a magnetized ternary Cross fluid over a stretching cylinder, and Chandel and Sharma [10] found that heat transfer falls as the magnetic influence grows in a ternary stagnation flow. Rafique et al. [11] separated the thermal and magnetic contributions to entropy production in an unsteady MHD hybrid flow. Effective-property choices can matter just as much: Akbar et al. [12] obtained different thermodynamic responses for aggregated and non-aggregated descriptions, and Khanafer and Vafai [13] showed that commonly used conductivity and viscosity models for nanofluids disagree markedly with one another and with measured data. Sahoo and Kumar [14] measured the viscosity of a ternary hybrid suspension, found that classical models did not reproduce the data, and fitted a new correlation. None of these systems is a validation case for the present film. They do show, however, that hydraulic cost and property-model uncertainty have to be resolved when the predicted thermal separation is small.

Magnetic ternary thin films, mono/hybrid comparisons, stratification, oscillatory forcing and data-assisted optimization have already been studied [15–18], and porous resistance and radiation have been added to viscoelastic Maxwell films on an unsteady stretching sheet [19]. Entropy calculations for radiative hybrid fluids have been reported for squeezed rotating disks and stretched three-dimensional flows [20–22], and second-law analyses now cover several hybrid and ternary rheologies with electromagnetic forcing [23–26]. Time-dependent stretching and shrinking solutions, together with hybrid-nanofluid films on an unsteady stretching sheet, show how boundary motion shapes the flow [27, 28], and in the original finite-film analysis the film thickness is itself part of the solution [29]. Our concern is the comparison used for the CuO-TiO_2-SiO_2/blood film of Maatki et al. [30]. Their ternary case has the largest wall heat-transfer response, but the mono, binary and ternary cases do not all have the same final solid fraction, so part of the reported separation is a loading effect.

We therefore ask whether the ternary suspension keeps a measurable thermal advantage when the mono, binary and ternary cases contain exactly the same solid volume, and how that advantage compares with the associated drag and modeling uncertainty. The question is relevant to thin-film heating and coating flows, in which wall heat transfer, traction and film thickness are coupled. The momentum and energy equations, free-surface conditions and constituent data of the Maatki et al. [30] model are kept; only the loading comparison is reformulated. At prescribed Φ all three suspensions contain the same total particle volume, so the Brinkman viscosity factor is common to them, while density, volumetric heat capacity and conductivity still depend on particle identity. Entropy production is evaluated from each converged velocity-temperature pair. Conductivity sensitivity is checked by comparing the multicomponent Bruggeman value with every sequential-Maxwell insertion order at the same final species fractions. Numerical error is assessed with Wang's finite-film benchmark, mesh refinement and a separate collocation code. The test is whether the ternary-minus-mono change in Nu^* survives equal loading and exceeds the numerical and conductivity-model variations.

2 Mathematical model and numerical method

2.1 Finite-film equations, equal loading and wall transport

The liquid occupies $0 \le y \le h(t)$ above the stretching surface. Because $h(t)$ is material and shear free, the transverse extent is an unknown of the hydrodynamic problem. The stretching velocity and magnetic field

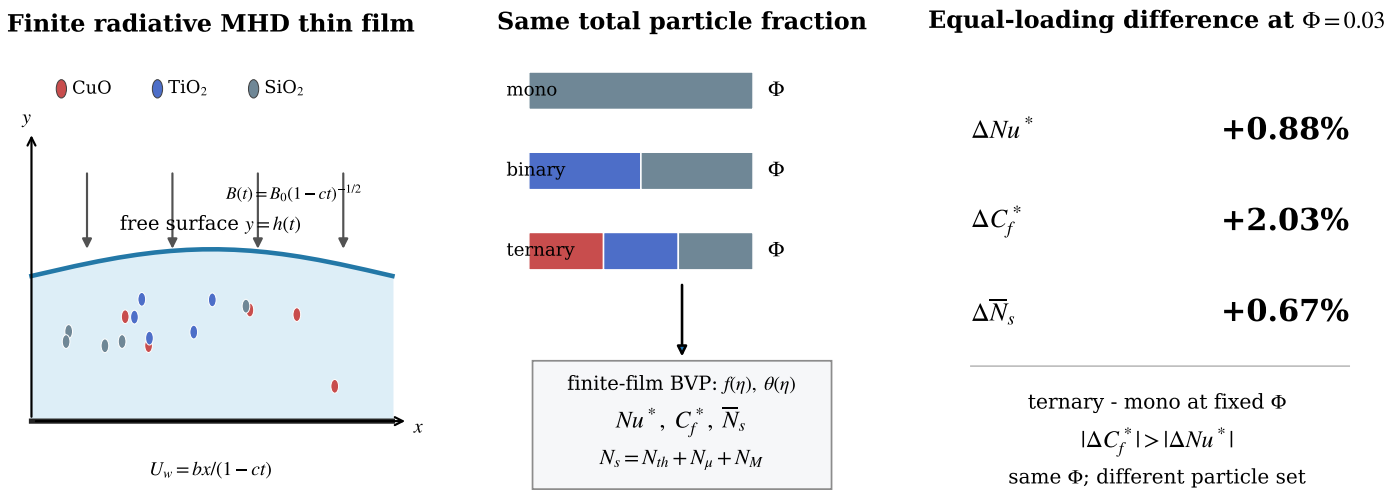

Figure 1. Finite-film geometry and equal-loading comparison. The mono, binary and ternary cases share the same total particle fraction Φ; each set of wall quantities is obtained from its own boundary-value solution.

are kept exactly as in the Maatki et al. [30] similarity formulation,

$$U_w(x,t) = \frac{bx}{1-ct}, \qquad B(t) = \frac{B_0}{\sqrt{1-ct}}, \qquad b > 0,\ c \geq 0. \tag{1}$$

Here b is the stretching-rate scale and c sets the imposed time dependence. The choice $B(t) \propto (1-ct)^{-1/2}$ is the one compatible with the similarity variables; it leaves a time-independent magnetic coefficient in the reduced momentum equation.

Following Maatki et al. [30], the suspension is treated as a homogeneous Newtonian effective medium. The film is incompressible and laminar, the particle fractions are spatially uniform, and particle slip, migration and agglomeration are excluded. The magnetic Reynolds number is small enough for the induced field to be neglected, and no pressure gradient is imposed. At the material free surface the tangential stress and normal heat flux vanish. The effective thermophysical properties follow from the mixture rules given below. Radiative transfer is represented by Rosseland diffusion, which assumes an optically thick grey medium. The T^4 term is kept without linearization, so the transverse radiative flux contributes the nonlinear $T^3 T_y$ term; optically thin or strongly scattering films are outside the scope of this approximation. Under these assumptions, the dimensional balances of the Maatki et al. [30] model are

$$u_x + v_y = 0, \tag{2}$$

$$u_t + uu_x + vu_y = \frac{\mu_{nf}}{\rho_{nf}} u_{yy} - \frac{\sigma_{nf} B^2(t)}{\rho_{nf}} u, \tag{3}$$

$$T_t + uT_x + vT_y = \frac{1}{(\rho C_p)_{nf}} \Big[k_{nf} T_{yy} + \frac{16\sigma^*}{3k^*} \frac{\partial}{\partial y}\big(T^3 T_y\big) + Q_0 (T - T_0) \Big]. \tag{4}$$

At the sheet, no slip and the imposed temperature are prescribed. The outer boundary is not fixed in advance: $h(t)$ is a material free surface determined by the solution. Zero tangential stress gives $u_y = 0$, the adiabatic-interface approximation gives $T_y = 0$, and the kinematic condition requires the interface normal velocity to equal $\mathrm{d}h/\mathrm{d}t$:

$$u = U_w, \quad v = 0, \quad T = T_s, \qquad y = 0, \tag{5}$$

$$u_y = 0, \quad T_y = 0, \quad v = \frac{\mathrm{d}h}{\mathrm{d}t}, \qquad y = h(t). \tag{6}$$

The wall temperature is

$$T_s(x,t) = T_0 - T_{\mathrm{ref}} \left(\frac{bx^2}{2\nu_f} \right) (1-ct)^{-3/2}. \tag{7}$$

The ratio $\theta_w = T_s/T_0$ is used as the local wall-temperature parameter in the reduced energy

equation; it is not a material property. The heated cases considered here ($\theta_w > 1$) correspond to $T_{\mathrm{ref}} < 0$ in Eq. (7). The geometry and the common-loading construction are sketched in Figure 1.

The numerical property set is that reported by Maatki et al. [30]. With ρ in $\mathrm{kg\,m^{-3}}$, C_p in $\mathrm{J\,kg^{-1}\,K^{-1}}$ and k in $\mathrm{W\,m^{-1}\,K^{-1}}$, the values (ρ, C_p, k) used in the code are blood (1063, 3594, 0.492), CuO (6320, 531.8, 76.5), TiO_2 (4230, 692, 8.4) and SiO_2 (2220, 745, 1.4).

Electrical conductivities of the individual constituents are not supplied with that property set, and introducing a separate database for this one coefficient would change the material basis of the Maatki et al. [30] model. The magnetic term is therefore carried in the composite form that survives the similarity reduction.

Let φ_j denote the final volume fraction of particle species j. The controlled loading is

$$\Phi = \sum_j \varphi_j. \tag{8}$$

The mono case assigns the full fraction to SiO_2. In the binary case TiO_2 and SiO_2 each occupy $\Phi/2$, and in the ternary case CuO, TiO_2 and SiO_2 each occupy $\Phi/3$. The particle identities change while the total solid volume does not. Density and volumetric heat capacity are evaluated from

$$\rho_{nf} = (1-\Phi)\rho_f + \sum_j \varphi_j \rho_j, \tag{9}$$

$$(\rho C_p)_{nf} = (1-\Phi)(\rho C_p)_f + \sum_j \varphi_j (\rho C_p)_j. \tag{10}$$

The same Φ is used in the Brinkman viscosity relation [31],

$$\mu_{nf} = \mu_f (1-\Phi)^{-2.5}. \tag{11}$$

Equation (11) makes $A_1 = \mu_{nf}/\mu_f$ identical for the three fluids at a given Φ. Any drag separation at common loading then comes from the remaining property coefficients and from the adjustment of the finite free surface, not from an extra viscosity multiplier assigned to the ternary mixture. A species-resolved viscosity correlation for this particular CuO-TiO_2-SiO_2/blood suspension is not available in the adopted property set.

Thermal conductivity is evaluated first with the symmetric multicomponent Bruggeman relation [32],

$$(1-\Phi)\frac{k_f - k_{nf}}{k_f + 2k_{nf}} + \sum_j \varphi_j \frac{k_j - k_{nf}}{k_j + 2k_{nf}} = 0. \tag{12}$$

A second calculation uses sequential Maxwell mixing [33] to measure the sensitivity to the construction of k_{nf},

$$k^+ = k^- \frac{k_p + 2k^- - 2\phi(k^- - k_p)}{k_p + 2k^- + \phi(k^- - k_p)}. \tag{13}$$

Here k^- is the conductivity of the mixture before species p is inserted, k_p is the conductivity of that species, ϕ is its insertion fraction and k^+ is the resulting conductivity. For each particle ordering, the intermediate insertion fractions are chosen to recover the same prescribed final φ_j, so changing the order changes only the path by which k_{nf} is assembled. The reduced property ratios are

$$A_1 = \frac{\mu_{nf}}{\mu_f}, \quad A_2 = \frac{\rho_{nf}}{\rho_f}, \quad A_3 = \frac{\sigma_{nf}}{\sigma_f},$$
$$A_4 = \frac{k_{nf}}{k_f}, \quad A_5 = \frac{(\rho C_p)_{nf}}{(\rho C_p)_f}. \tag{14}$$

Using the stream function ψ, the similarity variables are

$$\eta = \left[\frac{b}{\nu_f(1-ct)}\right]^{1/2} y,$$
$$\psi = x\left[\frac{\nu_f b}{1-ct}\right]^{1/2} f(\eta), \tag{15}$$
$$\theta = \frac{T - T_0}{T_s - T_0}, \quad u = \frac{bx}{1-ct} f'(\eta),$$
$$v = -\left[\frac{\nu_f b}{1-ct}\right]^{1/2} f(\eta). \tag{16}$$

The interface corresponds to $\eta = \zeta$, and ζ is solved together with the velocity field. Substitution into the momentum and energy balances gives

$$A_1 f''' + A_2\left[f f'' - S\left(\frac{\eta}{2} f'' + f'\right) - (f')^2\right] - M f' = 0, \tag{17}$$

$$\left(A_4 + Nr\chi^3\right)\theta'' + 3Nr\chi^2(\theta_w - 1)(\theta')^2$$
$$+ Pr A_5\left[f\theta' - 2f'\theta - \frac{S}{2}(3\theta + \eta\theta')\right] + Q^* Pr\,\theta = 0. \tag{18}$$

The temperature ratio χ and the dimensionless control parameters are

$$\chi = 1 + (\theta_w - 1)\theta = \frac{T}{T_0}, \quad S = \frac{c}{b}, \quad Nr = \frac{16\sigma^* T_0^3}{3k_f k^*},$$
$$M \equiv A_3\alpha, \quad \alpha = \frac{\sigma_f B_0^2}{\rho_f b}, \quad Pr = \frac{\nu_f (\rho C_p)_f}{k_f},$$
$$Q^* = \frac{Q_0(1-ct)}{b(\rho C_p)_f}. \tag{19}$$

The momentum equation contains $A_3\alpha$ only as a product. Since A_3 cannot be evaluated from the available constituent data, the product is denoted by M and varied directly; Q^* is constant when $Q_0 \propto (1-ct)^{-1}$. The wall and free-surface conditions reduce to

$$f(0)=0, \quad f'(0)=1, \quad \theta(0)=1,$$
$$f(\zeta)=\frac{S\zeta}{2}, \quad f''(\zeta)=0, \quad \theta'(\zeta)=0. \tag{20}$$

On the stretching-film branch $f''(0)<0$. We therefore report the positive wall-drag magnitude together with the reduced heat-transfer rate,

$$C_f^* = -A_1 f''(0), \qquad Nu^* = -\big(A_4 + Nr\theta_w^3\big)\theta'(0). \tag{21}$$

2.2 Second-law diagnostic, numerical solution and verification

The Maatki et al. [30] energy equation, Eq. (4), and hence its reduced form, Eq. (18), omit viscous and Joule heating. Adding either term would change the temperature boundary-value problem, so this is not done here. Eq. (18) is solved as stated, and entropy production is then evaluated from its temperature field and the corresponding velocity field. The viscous-deformation and magnetic-damping contributions therefore enter only the second-law diagnostic; their possible feedback on temperature is checked separately below.

With the same transverse-gradient approximation as the similarity model, the dimensional entropy-production rate is

$$\dot{s}'''_{gen} = \frac{k_{eff}(T)}{T^2}T_y^2 + \frac{\mu_{nf}}{T}u_y^2 + \frac{\sigma_{nf}B^2}{T}u^2,$$
$$k_{eff}(T) = k_{nf} + \frac{16\sigma^* T^3}{3k^*}. \tag{22}$$

After the transverse length is scaled with $L_y = [\nu_f(1-ct)/b]^{1/2}$, the entropy number separates into thermal, viscous and magnetic parts,

$$N_s = N_{th} + N_\mu + N_M, \tag{23}$$
$$N_{th} = \big(A_4 + Nr\chi^3\big)\frac{(\theta')^2}{\chi^2}, \tag{24}$$
$$N_\mu = \Lambda A_1 \frac{(f'')^2}{\chi}, \qquad N_M = \Lambda M \frac{(f')^2}{\chi}, \tag{25}$$
$$\Lambda = \frac{\mu_f b^2 x^2 T_0}{k_f (T_s - T_0)^2 (1-ct)^2}. \tag{26}$$

Both Λ and θ_w depend on x and t and are treated as independent local parameters. The local thermal fraction and its film-integrated counterpart are

$$Be = \frac{N_{th}}{N_s}, \qquad \overline{N}_i = \int_0^\zeta N_i \,\mathrm{d}\eta, \qquad \overline{Be} = \frac{\overline{N}_{th}}{\overline{N}_s}, \tag{27}$$

where i stands for th, μ, M or s; $\overline{Be}$ is shown in Figure S1(b) of the Supplementary Material.

To quantify the heating omitted from Eq. (18), the viscous and magnetic source can be written on the same scale as

$$D(\eta) = \Lambda(\theta_w - 1)\big[A_1 (f'')^2 + M(f')^2\big]. \tag{28}$$

We compare $\int D\,\mathrm{d}\eta$ with the integrated magnitude of the non-conductive terms already retained in Eq. (18). At the reference state the ratio is $\mathcal{R}_{diss} = 5.28\times10^{-4}$, and it does not exceed 1.32×10^{-3} for $0.002 \le \Lambda \le 0.05$ (Figure S1). The calculations below use $\Lambda = 0.02$. Over this interval the omitted dissipative source is about three orders of magnitude smaller than the retained thermal forcing, so the entropy terms are used as post-processed measures of irreversibility and are not fed back into the inherited temperature equation.

Two quantities are adjusted in the momentum shooting calculation: the wall curvature $f''(0)$ and the unknown endpoint ζ. Fourth-order Runge-Kutta (RK4) integration returns the residuals $f(\zeta) - S\zeta/2$ and $f''(\zeta)$, and a damped two-variable Newton step updates $f''(0)$ and ζ. Once the velocity solution has converged, a scalar shooting iteration adjusts $\theta'(0)$ until $\theta'(\zeta) = 0$. The boundary-residual norm must fall below 10^{-10}. The independently written collocation code reaches a nonlinear residual of order 10^{-14}. Uniform RK4 meshes contain 300-600 intervals in the production runs and 1200 intervals in the refinement check. Continuation is used only along the extended M and S sweeps, where it prevents unintended branch switching. Shooting is convenient because the free-surface location appears directly among the unknowns, although convergence can depend on the starting guess where branches become difficult; the collocation calculation provides an independent check in that case.

Three numerical checks were made. In the particle-free limit with magnetic forcing, radiation and volumetric heating removed, the equations reduce to Wang's finite stretching-film problem after the coordinate conversion used for the benchmark. The six values in Table 1 differ from Wang's $F''(0)$ by no more than

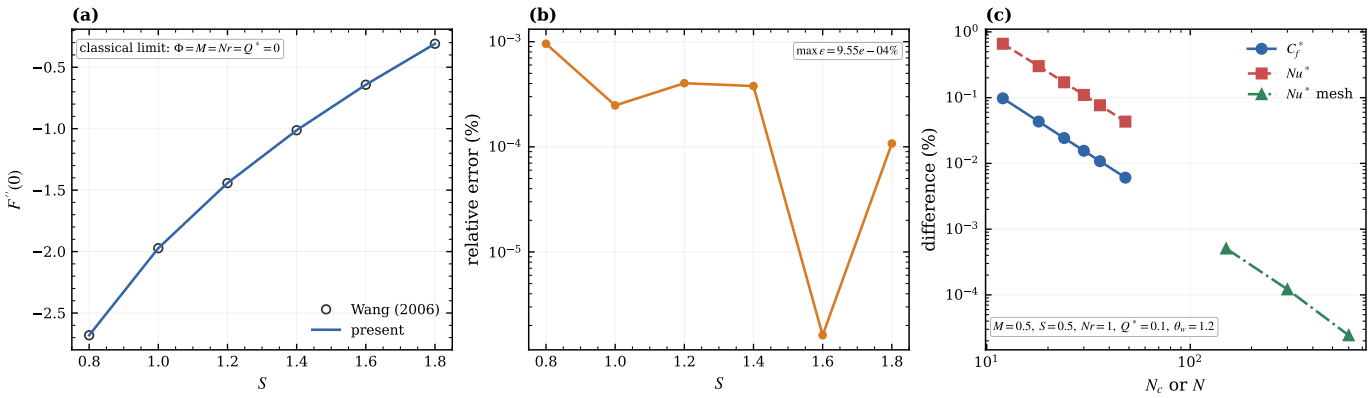

Figure 2. Numerical checks: (a) $F''(0)$ in the particle-free limit compared with Wang [2]; (b) relative error of that comparison; (c) collocation-shooting differences and RK4 mesh sensitivity.

9.55×10^{-4}%. The same boundary-value equations were also discretized by trapezoidal collocation and solved with a dense Newton iteration. At $N_c = 48$ the difference from shooting is 0.0061% in C_f^* and 0.0432% in Nu^*, with a nonlinear residual of order 10^{-14}. Checks at $(M, S) = (3, 0.5)$, $(0.5, 1.5)$ and $(0.5, 1.8)$ give maximum differences below 0.009% for drag and 0.013% for heat transfer (Table S2 in the Supplementary Material). Finally, increasing the RK4 mesh from 600 to 1200 intervals changes Nu^* by 2.43×10^{-5}% and leaves the reported digits of C_f^* unchanged (Table S1). Figure 2 summarizes these tests.

Table 1. Wall curvature for the particle-free finite-film limit used in the Wang [2] benchmark. Relative errors are computed from unrounded values.

S	Wang [2]	Present $F''(0)$	Relative error (%)
0.8	−2.680940	−2.680966	9.55×10^{-4}
1.0	−1.972380	−1.972385	2.48×10^{-4}
1.2	−1.442631	−1.442625	4.03×10^{-4}
1.4	−1.012784	−1.012780	3.78×10^{-4}
1.6	−0.642397	−0.642397	1.61×10^{-6}
1.8	−0.309137	−0.309137	1.08×10^{-4}

3 Results and discussion

Unless a parameter is being varied, the calculation uses $\Phi = 0.03$, $M = S = 0.5$, $Nr = 1$, $Pr = 6.2$, $Q^* = 0.1$, $\theta_w = 1.2$ and $\Lambda = 0.02$. The Prandtl number is prescribed as an independent dimensionless parameter and is not computed from the blood properties listed in Section 2.1.Loading results are discussed mainly up to $\Phi = 0.06$; the $\Phi = 0.08$ calculation is included as an upper-end check on the observed ordering. Profiles and integral measures come directly from Eqs. (17)-(27).

3.1 Composition at fixed solid loading

The equal-loading property ratios are plotted in Figure 3. At a given Φ, the Brinkman expression gives one value of A_1 for all three compositions. This is not so for A_2: adding the denser CuO raises the ternary density ratio above the binary and mono values. With the Bruggeman rule, the conductivity ratio A_4 follows the same ordering, and the six sequential-Maxwell constructions stay close to it. The volumetric heat-capacity ratio A_5 decreases with Φ, because each solid has a lower ρC_p than blood. The composition dependence left in Eq. (17) is thus carried by A_2, while in Eq. (18) it acts through A_4 and A_5.

At $\Phi = 0.03$ the reduced heat-transfer rate changes from $Nu^* = 6.15017$ for SiO_2/blood to 6.20435 for CuO-TiO_2-SiO_2/blood, an increase of 0.881%. The corresponding changes are 2.029% in C_f^* and 0.668% in $\overline{N}_s$. At $\Phi = 0.06$ the ternary-minus-mono changes become 1.907%, 3.929% and 1.486%, and at $\Phi = 0.08$ they are 2.680%, 5.130% and 2.123%. The absolute values are listed in Table 2. In Figure 4(d) the loading paths are plotted directly in the (C_f^*, Nu^*) plane. The ternary path gains heat transfer but moves faster toward larger drag; over the main loading interval its relative drag increase is roughly twice its relative heat-transfer increase.

The drag separation does not arise from the Brinkman viscosity factor, because at fixed Φ the value of A_1 is the same for all three suspensions. The composition dependence enters the momentum balance through A_2 instead. Changing A_2 alters the inertia-unsteadiness-diffusion balance and, through the kinematic boundary condition, the computed endpoint ζ; the associated change in $f''(0)$ produces the difference in C_f^*. The thermal response has a separate origin: A_4 changes the diffusive coefficient

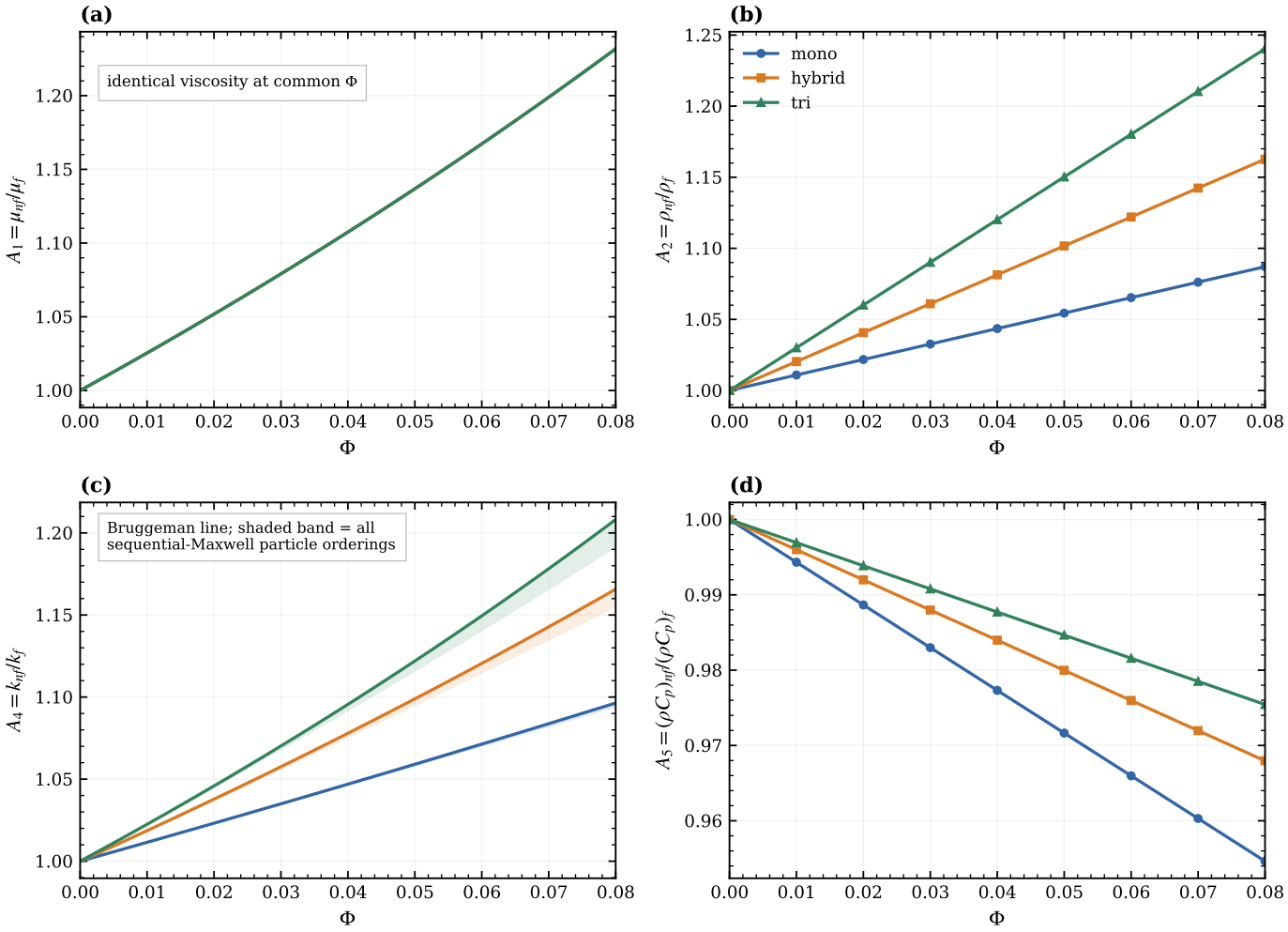

Figure 3. Property ratios at common total loading: (a) A_1, (b) A_2, (c) Bruggeman A_4 with the sequential-Maxwell ordering envelope and (d) A_5. In the legends, "hybrid" denotes the binary and "tri" the ternary suspension.

Table 2. Wall heat transfer, drag and integrated entropy at matched total particle fraction Φ.

Φ	Fluid	Nu^*	C_f^*	$\overline{N}_s$
0.03	SiO_2/blood	6.15017	1.43436	2.25478
	TiO_2-SiO_2/blood	6.18677	1.44880	2.26584
	CuO-TiO_2-SiO_2/blood	6.20435	1.46347	2.26983
0.06	SiO_2/blood	6.14575	1.50908	2.25791
	TiO_2-SiO_2/blood	6.22349	1.53863	2.28181
	CuO-TiO_2-SiO_2/blood	6.26293	1.56837	2.29146
0.08	SiO_2/blood	6.14320	1.56192	2.26031
	TiO_2-SiO_2/blood	6.25108	1.60195	2.29384
	CuO-TiO_2-SiO_2/blood	6.30782	1.64204	2.30829

in Eq. (18), whereas A_5 changes the convective and unsteady thermal terms. Fixing Φ removes the extra concentration contribution from both comparisons.

Because the 0.881% heat-transfer increment at $\Phi = 0.03$ is small, the conductivity construction has to be checked against it. We repeated the ternary calculation for all six sequential-Maxwell particle orders without changing the final species fractions. Relative to the Bruggeman result, the largest shift in Nu^* is 0.035% at $\Phi = 0.03$, 0.149% at 0.06 and 0.276% at 0.08 (Table 3). Each is smaller than the corresponding ternary-minus-mono increment, so the sign of the thermal change is not altered by the conductivity constructions tested here, although its magnitude remains modest.

3.2 Finite-film response to magnetic, unsteady and thermal forcing

The field solutions in Figure 5 help explain the wall trends. For the magnetic profiles we set $S = 0.3$, which keeps all interfaces beyond the plotted interval $0 \le \eta \le 4$. Starting from $f'(0) = 1$, the streamwise velocity decreases through the film and becomes smaller as M increases, and $|f''|$ tends to zero at the shear-free surface. The thermal profiles are evaluated at $M = 0.5$. Larger Nr raises θ in the film, while $|\theta'|$ tends to zero at the insulated interface.

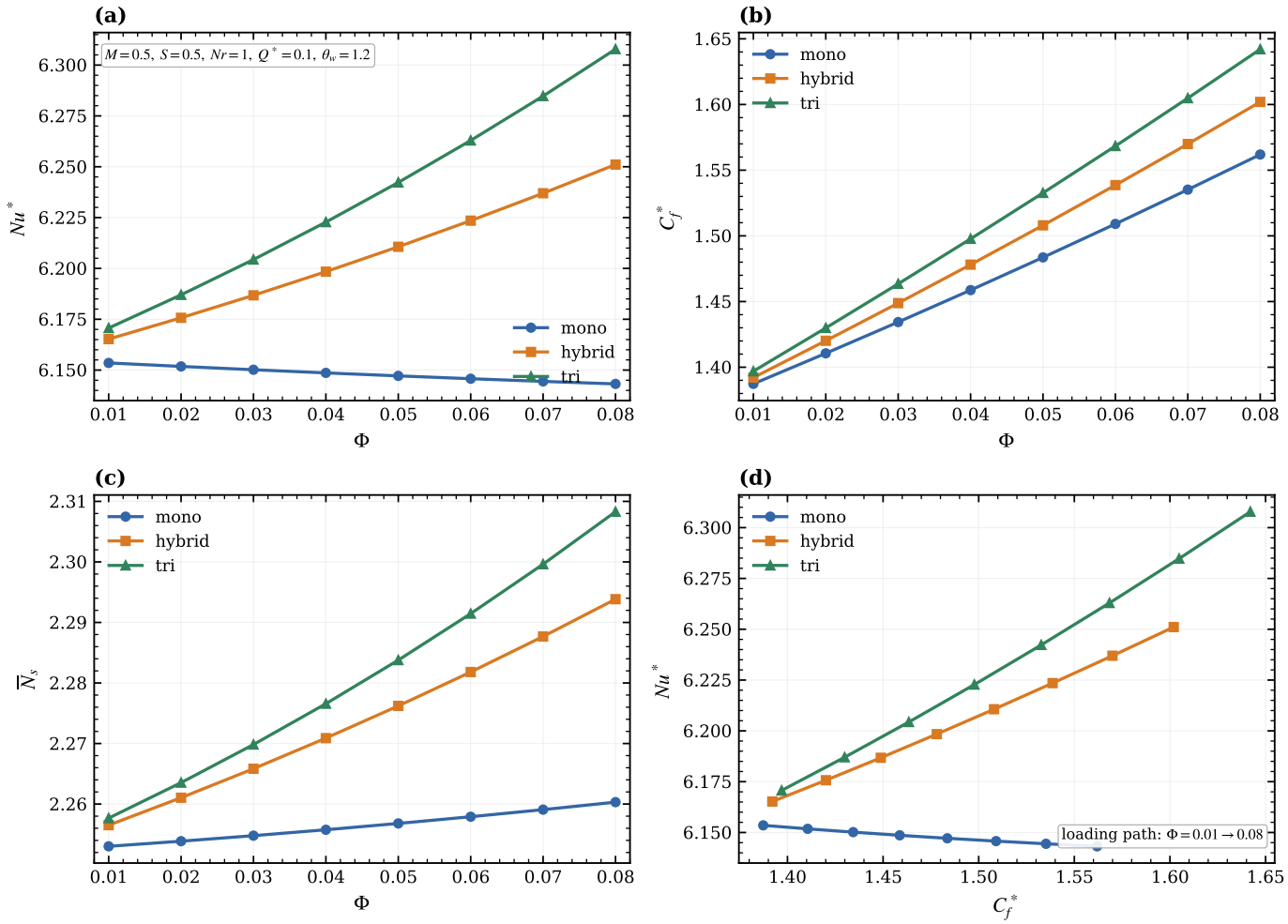

Figure 4. Equal-loading sweep over $0.01 \le \Phi \le 0.08$: (a) Nu^*, (b) C_f^*, (c) $\overline{N}_s$ and (d) the same states in the (C_f^*, Nu^*) plane.

Table 3. Ternary Nu^* from Bruggeman conductivity and from all sequential-Maxwell orderings at unchanged final composition.

Φ	Bruggeman A_4	Bruggeman Nu^*	Sequential Nu^*	Max. shift (%)
0.03	1.07021	6.20435	6.20217-6.20252	0.035
0.06	1.14949	6.26293	6.25356-6.25504	0.149
0.08	1.20817	6.30782	6.29038-6.29312	0.276

Changing M produces a far larger response than changing particle identity at fixed loading. Between $M = 0$ and 5, ζ falls from 3.8674 to 1.6643, while Nu^* falls by 9.996% and C_f^* rises by 109.28% (Figure 6(a,b)). This is consistent with the $-Mf'$ term in Eq. (17): magnetic damping reduces the streamwise velocity. In a finite film the material surface moves as well, because ζ is an unknown of the boundary-value problem, and the contracted solution has a larger $|f''(0)|$, which accounts for the rise in wall drag. Chandel and Sharma [10] also report lower heat transfer under magnetic forcing, although their stagnation-flow geometry permits a comparison of direction only.

Film thickness decreases throughout the S sweep, but the wall quantities do not vary monotonically (Figure 6(c,d)). The computed endpoint changes from $\zeta = 8.2035$ at $S = 0.2$ to 0.2188 at $S = 1.9$. Over the same range Nu^* increases from 5.7047 to 7.4921 at about $S = 1.5$ and then drops to 5.3870. The maxima of C_f^* and $\overline{N}_s$ occur earlier, near $S = 1.0$ and 1.1, respectively. For moderate unsteadiness the contracting film supports a steeper wall-temperature gradient. Near the high-S end the free surface approaches the sheet, the transverse domain becomes very short, and the velocity curvature and thermal field weaken. Separate collocation solutions at $S = 1.5$

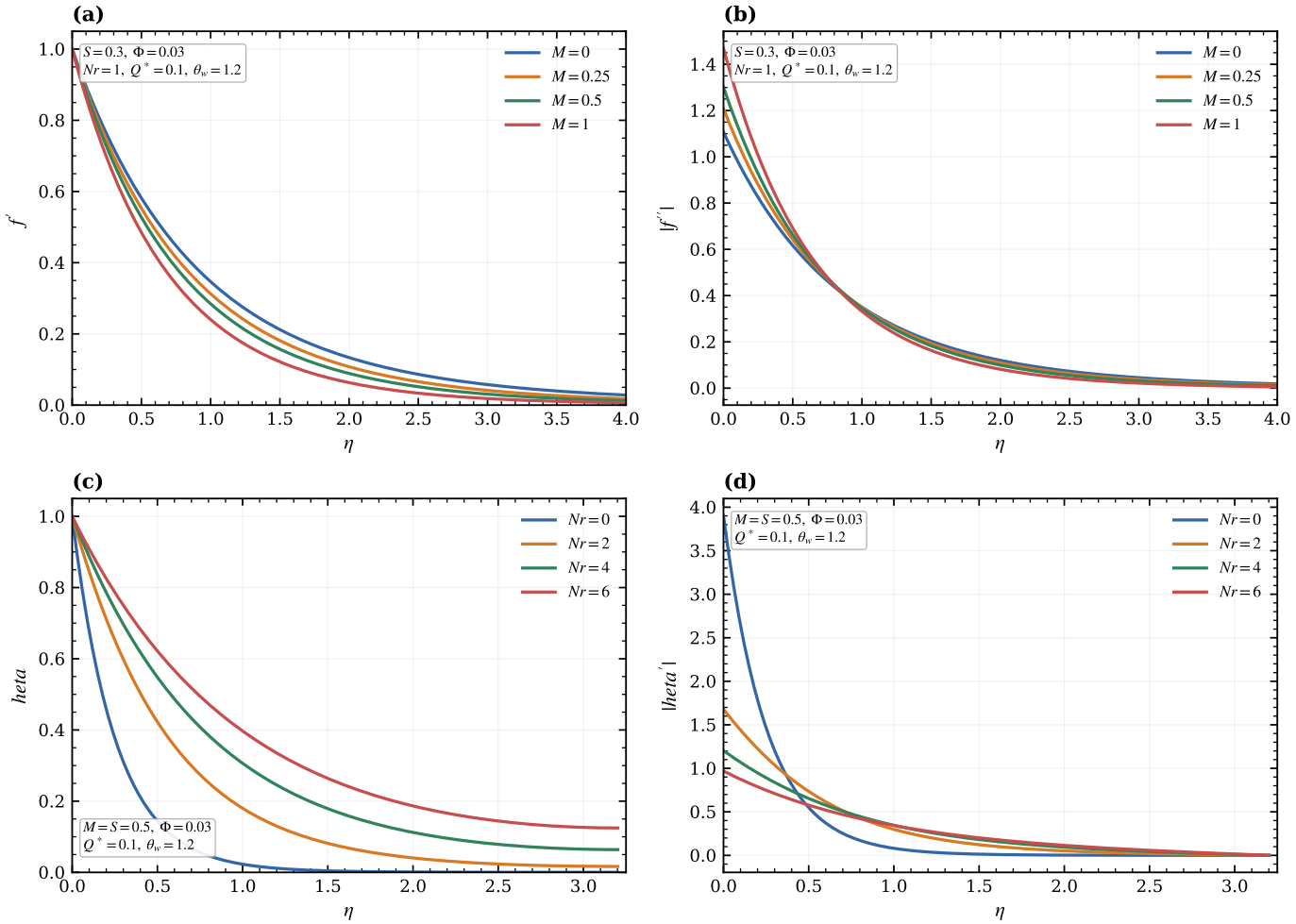

Figure 5. Finite-film profiles: (a) $f'(\eta)$ and (b) $|f''(\eta)|$ for $M = 0$, 0.25, 0.5 and 1 at $S = 0.3$; (c) $\theta(\eta)$ and (d) $|\theta'(\eta)|$ for $Nr = 0$, 2, 4 and 6.

and 1.8 follow the same non-monotone branch, so the reversal is not a continuation artifact of the shooting calculation.

Among the thermal parameters, Nr produces the widest change (Figure 7). Increasing it from 0 to 6 takes Nu^* from 4.1782 to 11.0797, a 165.18% increase, and raises $\overline{N}_s$ by 109.68%. In Eq. (18), Nr modifies both the coefficient $A_4 + Nr\chi^3$ and the nonlinear gradient term, and it also enters N_{th} through Eq. (24). The Q^* sweep acts in the opposite direction under the sign convention of Eq. (4): from -0.2 to 0.7, Nu^* decreases by 20.88% and $\overline{N}_s$ by 26.80%. Changing θ_w from 1.05 to 1.6 raises Nu^* by 30.28% but reduces $\overline{N}_s$ by 36.26%. This opposite movement is consistent with the temperature dependence of the entropy normalization, including the T^{-2} factor in Eq. (22).

3.3 Relative parameter influence and comparison with published trends

Percentage changes over a full sweep depend on the chosen endpoints, so the relative influence near the reference state was also measured with the logarithmic elasticity

$$E_y^p = \frac{p}{y}\frac{\partial y}{\partial p}, \tag{29}$$

evaluated at the reference state for the ternary suspension. The derivative was computed with centred perturbations of 1, 2 and 4%, and their spread is shown in Figure 8. For Nu^* the elasticities are 0.573 for θ_w, 0.260 for Nr and 0.130 for S, whereas $E^{\Phi}_{Nu^*} = 0.00864$. The drag elasticities with respect to M and S are 0.127 and 0.0957, compared with 0.0695 for Φ. For $\overline{N}_s$ the largest local responses occur for θ_w, Nr and S. The local calculation therefore agrees with the wider sweeps in that Φ has the smallest elasticity among the parameters listed, for both Nu^* and C_f^*. The ranking among θ_w, Nr and S differs from that of the full-range percentages, because the full-range values depend on the chosen endpoints.

The joint (Nr, Φ) calculation consists of 117 converged boundary-value solutions for $0.005 \le \Phi \le 0.08$ and $0 \le Nr \le 6$. Before contouring, each state was checked

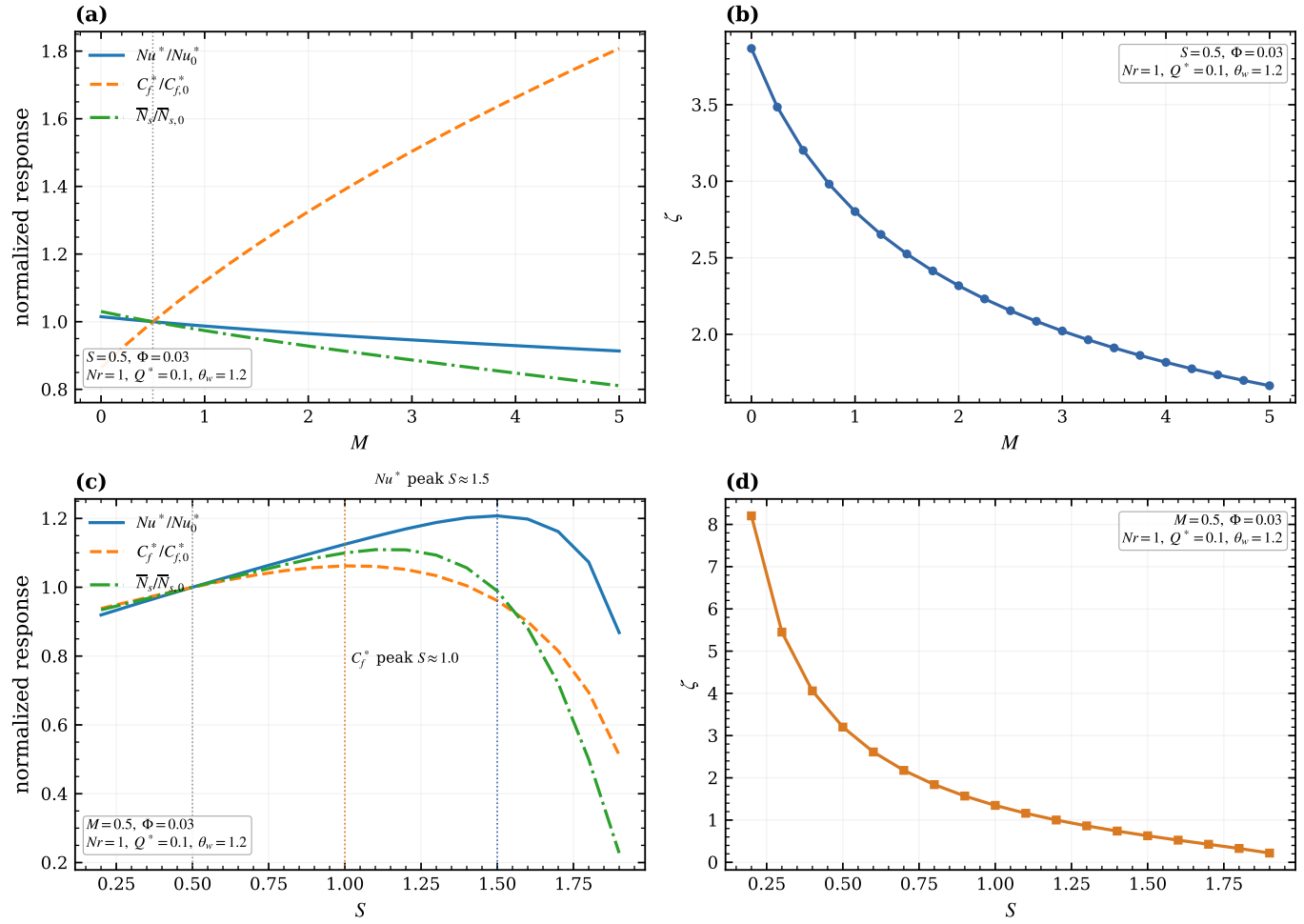

Figure 6. Magnetic and unsteady sweeps: (a) normalized wall response and (b) ζ for $0 \le M \le 5$; (c) normalized wall response and (d) ζ for $0.2 \le S \le 1.9$.

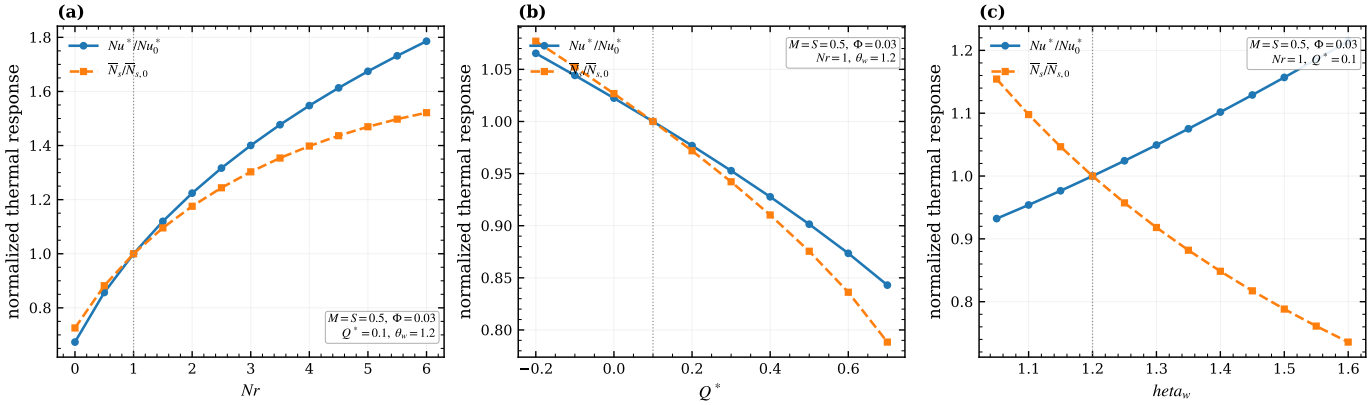

Figure 7. Normalized thermal response to separate variations of (a) Nr, (b) Q^* and (c) θ_w; the remaining parameters are stated in each panel.

for finite fields, $0 \le \theta(\eta) \le 1$, $Nu^* > 0$ and $\overline{N}_s > 0$, and Figure 9 interpolates only the accepted points. At every point of this grid the ternary Nu^* exceeds the mono value, by about 0.034% to 5.51%. The drag difference does not depend on Nr because the momentum equation has no thermal coupling. Entropy does not keep a single ordering: $\Delta\overline{N}_s$ spans approximately -0.60% to 4.78% and changes sign within the mapped range. Radiation can thus reverse the mono-ternary ordering of the integrated entropy measure while the heat-transfer difference stays positive.

Table 4 sets the computed trends beside published results; it is not used as a numerical benchmark. The entropy-generation calculations for radiative hybrid

Table 4. Published results used for trend comparison. Different geometries are listed for physical context, not as numerical benchmarks.

Study	Configuration	Reported behavior	Connection with the present calculation
Jan et al. [9]	Magnetized Cross ternary flow over a cylinder	Drag and forced convection vary with magnetic forcing	Related transport-drag response
Chandel and Sharma [10]	Ternary stagnation flow	Stronger magnetic influence reduces heat transfer	Same sign of the magnetic heat-transfer trend
Rafique et al. [11]	Unsteady MHD hybrid flow	Magnetic and thermal controls alter entropy production	Related source-resolved second-law behavior
Maatki et al. [30]	CuO-TiO_2-SiO_2/blood film	Ternary suspension gives the largest thermal response	Ranking remains positive at equal loading; $\Delta Nu^* = 0.881\%$ at $\Phi = 0.03$
Hussein et al. [34]	Ternary hybrid disk flow	Particle addition changes drag more strongly than heat transfer	Qualitatively similar drag penalty
Khanafer and Vafai [13]	Review of nanofluid property data and models	Conductivity and viscosity models differ markedly from each other and from measurements	Motivates the conductivity-construction check (Table 3)

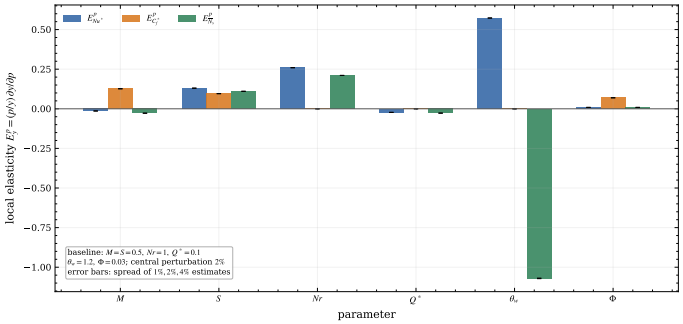

Figure 8. Logarithmic elasticities at the reference state. Bars are based on the 2% central difference; error bars span the estimates obtained with 1, 2 and 4% perturbations.

fluids in Refs. [20–22] use other geometries, carrier fluids and loading conventions. Jan et al. [9] is useful for the magnetic dependence of drag and heat transfer in ternary flows, Chandel and Sharma [10] for the sign of the magnetic heat-transfer trend, and Rafique et al. [11] for the separation of entropy sources in an unsteady MHD problem. Khanafer and Vafai [13] document how widely effective-property models can differ. The finite-film equations used here are those of Maatki et al. [30]; the change made in this work is the equal-Φ comparison. Hussein et al. [34] report a related hydraulic observation in disk flow, where the drag response to particles exceeds the heat-transfer response. Our comparison stays within one film model: only composition is varied, and the resulting Nu^* separation is set against the numerical and conductivity-model variations.

The model still carries the restrictions of a homogeneous effective medium. The adopted data set contains no measured viscosity or conductivity for the exact CuO-TiO_2-SiO_2/blood suspension, blood is represented as Newtonian, and the inherited energy equation omits viscous and magnetic heating. Electrical conductivity is not introduced as a separate constituent property, so its effect remains inside the composite parameter M. These points limit any absolute experimental reading of the calculated values. They affect the composition comparison less directly, because every case uses the same equations, mixture rules and total particle fraction; on that common basis the ternary-mono difference in Nu^* is still larger than the numerical mismatch and the conductivity-construction spread.

4 Conclusions

With the total particle fraction held fixed, replacing SiO_2/blood by CuO-TiO_2-SiO_2/blood at $\Phi = 0.03$ changes Nu^* by $+0.881\%$, C_f^* by $+2.029\%$ and $\overline{N}_s$ by $+0.668\%$, so the heat-transfer gain comes with a larger relative drag increase. Recomputing the ternary case with all six sequential-Maxwell insertion orders does not change the sign of ΔNu^*, and the resulting conductivity spread stays below the ternary-mono difference. At the reference state, the independent collocation check differs from shooting by at most 0.0432% on the production grid, well below the 0.881% increment.

The parameter sweeps put this composition effect in scale. From $M = 0$ to 5, C_f^* increases by 109.28% as

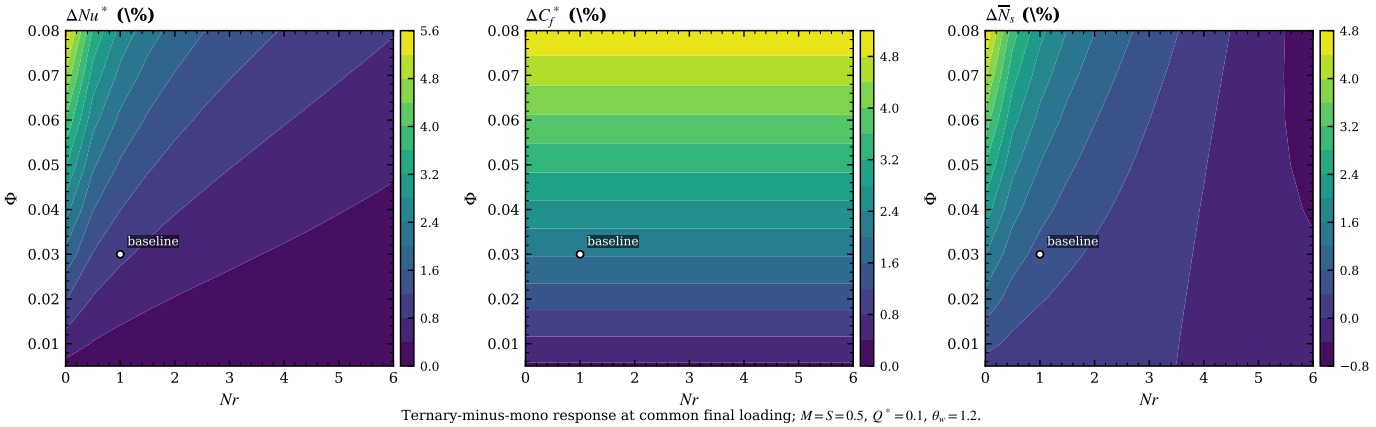

Figure 9. Ternary-minus-mono differences on the 117-state (Nr, Φ) grid: (a) ΔNu^*, (b) ΔC_f^* and (c) $\Delta \overline{N}_s$.

the film contracts. From $Nr = 0$ to 6, Nu^* rises from 4.1782 to 11.0797 (165.18%). The S sweep develops maxima because changing unsteadiness also moves the solved free surface. These responses are much larger than the 0.881% thermal change obtained by particle substitution at $\Phi = 0.03$. Within the present homogeneous Newtonian effective-medium model, the main variation of the film solution is associated with magnetic forcing, radiation and free-surface motion rather than with composition at fixed total loading.

Data Availability Statement

Data will be made available on reasonable request.

Funding

This work was supported without any funding.

Conflicts of Interest

The author declares no conflicts of interest.

AI Use Statement

The authors declare that ChatGPT-5 was used for language refinement and grammatical improvement of the manuscript. The authors have carefully reviewed, revised, and verified the AI-assisted output and take full responsibility for the content of the manuscript.

Ethical Approval and Consent to Participate

Not applicable. This is a purely computational study and involves no human participants or animals.

References

[1] Andersson, H. I., Aarseth, J. B., & Dandapat, B. S. (2000). Heat transfer in a liquid film on an unsteady stretching surface. *International Journal of Heat and Mass Transfer, 43*(1), 69-74. [CrossRef]

[2] Wang, C. (2006). Analytic solutions for a liquid film on an unsteady stretching surface. *Heat and Mass Transfer, 42*(8), 759-766. [CrossRef]

[3] Liu, I.-C., & Andersson, H. I. (2008). Heat transfer in a liquid film on an unsteady stretching sheet. *International Journal of Thermal Sciences, 47*(6), 766-772. [CrossRef]

[4] Abel, M. S., Mahesha, N., & Tawade, J. (2009). Heat transfer in a liquid film over an unsteady stretching surface with viscous dissipation in presence of external magnetic field. *Applied Mathematical Modelling, 33*(8), 3430-3441. [CrossRef]

[5] Noor, N. F. M., & Hashim, I. (2010). Thermocapillarity and magnetic field effects in a thin liquid film on an unsteady stretching surface. *International Journal of Heat and Mass Transfer, 53*(9-10), 2044-2051. [CrossRef]

[6] Liu, I. C., Wang, H. H., & Umavathi, J. C. (2013). Effect of viscous dissipation, internal heat source/sink, and thermal radiation on a hydromagnetic liquid film over an unsteady stretching sheet. *Journal of Heat Transfer, 135*(3), 031701. [CrossRef]

[7] Rabby, M. I. I., Uddin, M. W., Hassan, N. M. S., Al Nur, M., Uddin, R., Istiaque, S., & Abir, M. M. M. (2024). Recent progresses in tri-hybrid nanofluids: A comprehensive review on preparation, stability, thermo-hydraulic properties, and applications. *Journal of Molecular Liquids, 408*, 125257. [CrossRef]

[8] Mousavi, M., Pouranfard, A., & Darvishi, P. (2024). Experimental study and modeling of thermal and rheological characteristics of water-based CuO/CaCO3/SiO2 ternary hybrid nanofluid. *Colloids and Surfaces A: Physicochemical and Engineering Aspects, 686*, 133367. [CrossRef]

[9] Jan, A., Mushtaq, M., & Hussain, M. (2024). Heat transfer enhancement of forced convection

magnetized cross model ternary hybrid nanofluid flow over a stretching cylinder: non-similar analysis. *International Journal of Heat and Fluid Flow, 106*, 109302. [CrossRef]

[10] Chandel, S., & Sharma, D. (2024). Ternary nanofluid dynamics in stagnated flow with exponential heat and inclined magnetic field: Applications in advanced cooling and aerospace system. *International Journal of Heat and Fluid Flow, 109*, 109508. [CrossRef]

[11] Rafique, K., Mahmood, Z., Khan, U., Muhammad, T., Mir, A., Aich, W., & Kolsi, L. (2024). Unsteady MHD flow analysis of hybrid nanofluid over a shrinking surface with porous media and heat generation: computational study on entropy generation and Bejan number. *International Journal of Heat and Fluid Flow, 107*, 109419. [CrossRef]

[12] Akbar, Y., Li, K., Iqbal, J., Yang, X., & Mao, X. (2026). Thermodynamic analysis of nanofluid with aggregated and non-aggregated nanoparticles. *International Journal of Heat and Fluid Flow, 118*, 110205. [CrossRef]

[13] Khanafer, K., & Vafai, K. (2011). A critical synthesis of thermophysical characteristics of nanofluids. *International Journal of Heat and Mass Transfer, 54*(19-20), 4410-4428. [CrossRef]

[14] Sahoo, R. R., & Kumar, V. (2020). Development of a new correlation to determine the viscosity of ternary hybrid nanofluid. *International Communications in Heat and Mass Transfer, 111*, 104451. [CrossRef]

[15] Ullah, A. Z., Guo, X., Gul, T., Ali, I., Saeed, A., & Galal, A. M. (2023). Thin film flow of the ternary hybrid nanofluid over a rotating disk under the influence of magnetic field due to nonlinear convection. *Journal of Magnetism and Magnetic Materials, 573*, 170673. [CrossRef]

[16] Sreelakshmi, K., Mary, G. L. R., Alqsair, U. F., Elsemary, I. M., Alsayegh, R., Khan, S. U., & Kolsi, L. (2024). Evaluation of heat transfer for unsteady thin film flow of mono and hybrid nanomaterials with five different shape features. *Case Studies in Thermal Engineering, 62*, 105168. [CrossRef]

[17] Kavitha, L., Rehman, K. U., Varma, S. V. K., Shatanawi, W., Kumar, G. V., & Asghar, Z. (2025). Parametric analysis for thermally magnetized hybrid ternary (TMHT) nanofluid flow on thin film with temperature stratification. *International Journal of Thermofluids, 26*, 101089. [CrossRef]

[18] Wang, J., Kumar, M. D., Mamatha, S. U., Jithendra, T., Kouki, M., & Shah, N. A. (2025). Deep learning-based Adam optimization for magnetohydrodynamics radiative thin film flow of ternary hybrid nanofluid with oscillatory boundary conditions. *Chaos, Solitons & Fractals, 196*, 116448. [CrossRef]

[19] Waheed, S. E. (2016). Flow and heat transfer in a Maxwell liquid film over an unsteady stretching sheet in a porous medium with radiation. *SpringerPlus, 5*(1), 1061. [CrossRef]

[20] Sohail, M., Waseem, F., Abodayeh, K., & Rafique, E. (2026). Analysis of entropy generation on Darcy-Forchheimer squeezed hybrid nanofluid flow between two parallel rotating disks by considering thermal radiation and viscous dissipation. *Numerical Heat Transfer, Part B: Fundamentals, 87*(1), 2391501. [CrossRef]

[21] Waseem, F., Sohail, M., Sarhan, N., Awwad, E. M., & Khan, M. J. (2024). Utilization of OHAM to investigate entropy generation with a temperature-dependent thermal conductivity model in hybrid nanofluid using the radiation phenomenon. *Open Physics, 22*(1), 20240059. [CrossRef]

[22] Waseem, F., Sohail, M., & Singh, A. (2024). Entropy analysis of three-dimensional stretched magnetized hybrid nanofluid with thermal radiation and heat generation. *BioNanoScience, 14*(2), 547-565. [CrossRef]

[23] Jazaa, Y., Rehman, S., & Albouchi, F. (2024). On the enhancement of heat transport and entropy generation of the thin film flow of partially ionized non-Newtonian hybrid nanofluid. *Journal of the Taiwan Institute of Chemical Engineers, 157*, 105412. [CrossRef]

[24] Sindhu, T., & Jagadeeshkumar, K. (2025). Entropy generation and regression analysis of unsteady Carreau ternary hybrid nanofluid flow with electromagnetic and thermal influences. *Discover Nano, 20*(1), 231. [CrossRef]

[25] Pavuldass, P., & Reddy, P. B. A. (2026). Entropy generation and response surface analysis of tri-hybrid casson nanofluid with nonlinear radiation over a rotating disk. *Discover Nano, 21*(1), 357. [CrossRef]

[26] Abdul Hakeem, A. K., Shafiq, A., Parimala, P. M., Ragupathi, P., Ganga, B., Sindhu, T. N., Iqbal, M. A., & Ali, S. (2026). Thermodynamic irreversibility in ternary hybrid nanofluid flow over a curved stretching sheet with thermal dissipation effects. *Results in Engineering, 30*, 110191. [CrossRef]

[27] Turkyilmazoglu, M. (2024). Two models on the unsteady heat and fluid flow induced by stretching or shrinking sheets and novel time-dependent solutions. *ASME Journal of Heat and Mass Transfer, 146*(10), 101802. [CrossRef]

[28] Naganthran, K., Hashim, I., Nazar, R., Jalaluddin, D. A., & Aruchunan, E. (2023). Thermocapillarity in Cross hybrid nanofilm flow past an unsteady stretching sheet. *Coatings, 13*(4), 702. [CrossRef]

[29] Wang, C. Y. (1990). Liquid film on an unsteady stretching surface. *Quarterly of applied Mathematics, 48*(4), 601-610. [CrossRef]

[30] Maatki, C., Khan, S. U., Selimefendigil, F., & Kolsi, L. (2025). Artificial neural network-guided heat transfer analysis for thin film flow of tri-hybrid nanofluid under realistic thermal constraints: Advanced energy applications. *Case Studies in Thermal Engineering, 74*, 106975. [CrossRef]

[31] Brinkman, H. C. (1952). The viscosity of concentrated suspensions and solutions. *Journal of chemical physics, 20*(4), 571-571. [CrossRef]

[32] Bruggeman, D. A. G. (1935). Berechnung verschiedener physikalischer Konstanten von heterogenen Substanzen. I. Dielektrizitätskonstanten und Leitfähigkeiten der Mischkörper aus isotropen Substanzen. *Annalen der Physik, 416*(7), 636-664. [CrossRef]

[33] Maxwell, J. C. (1873). *A Treatise on Electricity and Magnetism*. Oxford: Clarendon Press. https://www.aproged.pt/biblioteca/MaxwellI.pdf

[34] Hussein, U. N., Khashi'ie, N. S., Arifin, N. M., & Pop, I. (2025). Heat transfer and flow dynamics of ternary hybrid nanofluid over a permeable disk under magnetic field and Joule heating effects. *Frontiers in Heat and Mass Transfer, 23*(2), 383-395. [CrossRef]

Appendix A. Derivation details

Similarity reduction. The definitions in Eqs. (15)-(16) satisfy the continuity equation identically. Substituting their derivatives into Eqs. (3) and (4) gives Eqs. (17) and (18). With $B(t) \propto (1-ct)^{-1/2}$, the time factors in the Lorentz term reduce to the constant coefficient M in Eq. (17).

Appendix B. Equal-loading properties

The final φ_j are prescribed before the conductivity calculation. For a chosen sequential-Maxwell order, the intermediate addition fractions are obtained recursively so that the specified final fractions are recovered. A permutation changes the conductivity construction, not Φ or the final composition.

Appendix C. Entropy scaling

Insert $T = T_0\chi$, $T_y = (T_s - T_0)\theta'/L_y$ and the similarity expression for u_y into Eq. (22), then divide by the reference entropy-production scale $k_f(T_s - T_0)^2/(T_0^2 L_y^2)$. The resulting thermal, viscous and magnetic terms are Eqs. (24)-(25). The magnetic contribution contains the same composite M as the momentum equation.

Appendix D. Dissipative-heating check

Equation (28) is evaluated only after the velocity and temperature fields have converged, and its integral is not fed back into Eq. (18). The normalized ratio does not exceed 1.32×10^{-3} over the tested Λ interval; individual values are shown in Figure S1 of the Supplementary Material.

Appendix E. Radiation-loading grid

Each (Nr, Φ) pair is solved as a separate boundary-value problem. A state is retained when the fields are finite, $Nu^* > 0$, $\overline{N}_s > 0$ and $0 \le \theta(\eta) \le 1$ throughout the film. Contours are constructed only after this pointwise filtering.

Supplementary Material

S1. Mesh refinement of the shooting calculation

The mesh test uses the reference state $\Phi = 0.03$, $M = S = 0.5$, $Nr = 1$, $Pr = 6.2$, $Q^* = 0.1$, $\theta_w = 1.2$ and $\Lambda = 0.02$. Table S1 lists the endpoint and wall quantities as the RK4 grid is doubled. Between 600 and 1200 intervals Nu^* changes by $2.43 \times 10^{-5}\%$, and the displayed digits of C_f^* do not change. For Nu^* the successive changes shrink by a factor of about four per doubling, so its observed order of convergence is close to two and not the nominal fourth order of RK4; the changes are nevertheless far below the 0.881% composition effect.

Table S1. RK4 mesh refinement at the reference state.

N	ζ	Nu^*	C_f^*
150	3.2020537953	6.2043776353	1.4634686183
300	3.2020537929	6.2043536531	1.4634686169
600	3.2020537928	6.2043476237	1.4634686168
1200	3.2020537928	6.2043461143	1.4634686168

S2. Independent collocation checks away from the reference state

The second solver uses collocation on a fixed interval instead of shooting. Table S2 compares the two codes at stronger magnetic forcing and at two states on the non-monotone unsteady branch. Away from the reference state the drag difference is below 0.009% and the heat-transfer difference below 0.013%. All rows of Table S2 use the same $N_c = 36$ grid; the baseline comparison reported in the main text was repeated at $N_c = 48$.

S3. Dissipative-heating scale

Viscous and magnetic dissipation are evaluated from the converged parent fields. They contribute to the entropy balance but are not inserted into the inherited temperature equation. Figure S1 gives $\mathcal{R}_{diss}$ over the

Table S2. Collocation-shooting comparison at four parameter states ($N_c = 36$).

Case	M	S	ζ_{coll}	ζ_{shoot}	ΔC_f^* (%)	ΔNu^* (%)
Baseline	0.5	0.5	3.20096384	3.20205379	0.01080	−0.07660
High M	3.0	0.5	2.02166494	2.02193290	0.00516	−0.01275
Near Nu^* maximum	0.5	1.5	0.62799186	0.62795007	0.00774	−0.00126
Thin-film branch	0.5	1.8	0.32771368	0.32768497	0.00888	0.00487

tested Λ range; its largest value, 1.32×10^{-3}, occurs at $\Lambda = 0.05$.

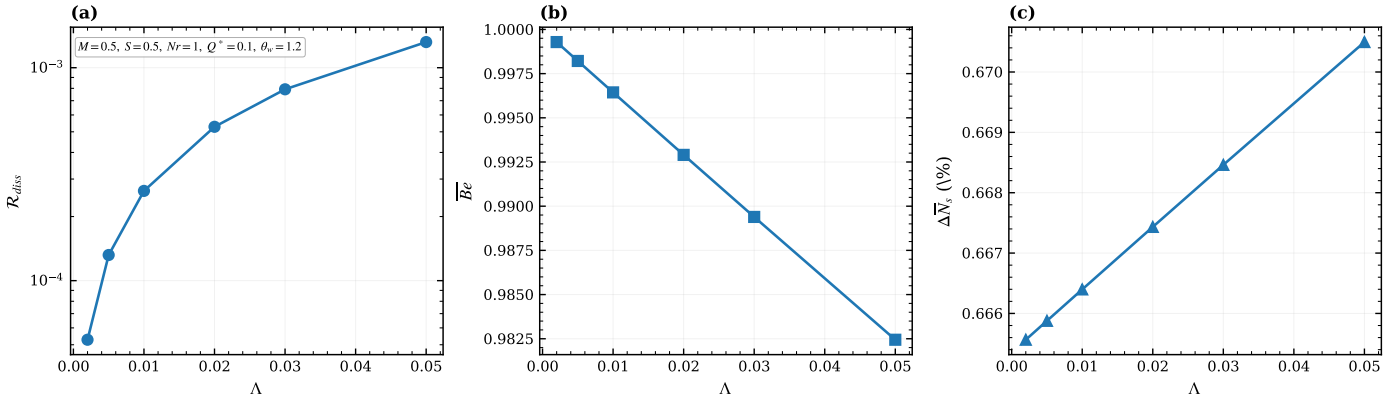

Figure S1. Dependence of (a) the omitted-source ratio $\mathcal{R}_{diss}$, (b) $\overline{Be}$ and (c) the ternary-minus-mono $\Delta\overline{N}_s$ on Λ.



Muhammad Riaz Khan received the B.S. degree in applied mathematics from Quaid-i-Azam University, Islamabad, Pakistan, in 2017, the M.S. degree in applied mathematics from the same university in 2019, and the Ph.D. degree in computational mathematics from the University of Chinese Academy of Sciences, China, in 2024. From 2024 to 2026 he was a postdoctoral researcher in the School of Chemistry and Chemical Engineering, Shanghai Jiao Tong University, China, working on computational fluid dynamics and multiphase-flow simulation of fluidized-bed chemical vapor deposition. He is currently a postdoctoral researcher in the Department of Mathematics, King Fahd University of Petroleum and Minerals, Saudi Arabia. His research covers Newtonian and non-Newtonian fluid mechanics, nanofluid flows, heat and mass transfer, multiphase flow and numerical modeling. (Email: mrkhan.math@gmail.com)

Noor Aslam Khan received the B.S. degree in applied mathematics from Quaid-i-Azam University, Islamabad, Pakistan, in 2016, and the M.S. degree in applied mathematics from the same university in 2018. Since 2019 he has been a Lecturer in Mathematics at Government Postgraduate College, Lakki Marwat, Khyber Pakhtunkhwa, Pakistan. He is currently on study leave and is working toward the Ph.D. degree in mathematics at Beijing Institute of Technology, Beijing, China. (Email: na.math.qau@gmail.com)